ACS APPLIED MATERIALS & INTERFACES

Research Article

www.acsami.org

Carbon-Anchored MnO Nanosheets as an Anode for High-Rate and Long-Life Lithium-Ion Batteries

Ying Xiao and Minhua Cao*

Key Laboratory of Cluster Science, Ministry of Education of China, Beijing Key Laboratory of Photoelectronic/Electrophotonic Conversion Materials, Department of Chemistry, Beijing Institute of Technology, Beijing 100081, P. R. China

Supporting Information

ABSTRACT: Developing electrode materials with high rate as well as prolonged cycle is particularly necessary for the ever-growing market penetration of electric vehicles and hybrid electric vehicle. Herein, we demonstrate a facile and efficient strategy to synthesize MnO/C hybrid via freeze-drying followed by thermal treatment in N_2 atmosphere. The MnO nanosheets are firmly anchored onto carbon layers to form MnO/C hybrid. When used as an anode in lithium-ion batteries, the typical MnO/C hybrid displays a high initial Coulombic efficiency of 83.1% and delivers a high capacity of 1449.8 mAh g^{-1} after 100 cycles at 0.3 A g^{-1}. Furthermore, the typical MnO/C hybrid can still maintain significantly high capacity of 1467.0 mAh g^{-1} after 2000 cycles at 5 A g^{-1}, which may be the best performance reported so far for MnO-based materials. The superior electrochemical performance of the MnO/C hybrid may be attributed to its unique microstructure features such as effective conductive pathway of carbon sheets, firm connection between MnO and carbon sheets, and small-sized MnO.

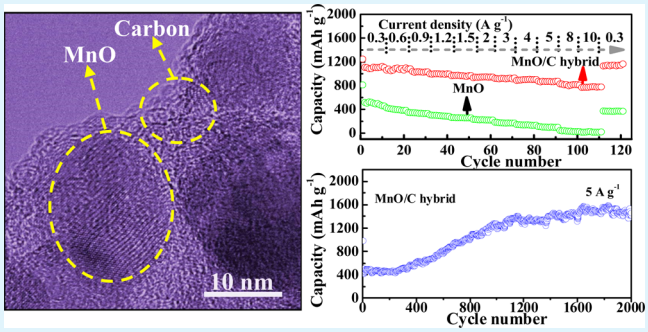

KEYWORDS: *MnO, freeze-drying, high-rate, anode materials, lithium-ion batteries*

1. INTRODUCTION

Low-dimensional nanostructured materials including nanoparticles (NPs), nanosheets (NSs) and nanowires have shown a competitive superiority in lithium-ion batteries (LIBs).[1−4] By the merits of large surface area and miniscule atomic scale thicknesses, two-dimensional (2D) NSs, such as graphene and transitional metal oxides, have attracted tremendous attention in the fundamental scientific areas and display a wide potential for many technological applications because of their fascinating mechanical, electrical, and optical properties.[1,5,6] When used as anode materials in LIBs, the unique structural and mechanical strength could endow the sheet-structured materials with excellent stability to alleviate the structure and volume changes of the electrodes generated during the intercalation−deintercalation process. Similar to NPs, NSs also can reduce the Li-ion diffusion length and display large contact interface, thus enhancing the reaction kinetics efficiently.[1,2] Thus far, considerable efforts have been made to design NS/NP-based materials to obtain highly efficient lithium-storage materials. For instance, Huang et al. synthesized BiOI nanosheets using commercial BiI_3 powder and demonstrated that the resultant material displayed significant potential as high-energy anode material for LIBs.[2] Cheng et al. reported the synthesis of NiO nanosheet/graphene composites by a hydrothermal reaction and related electrochemical measurements demonstrated the superior lithium-storage performance because of the synergistic effect between NiO NSs and graphene.[7] Lou's group prepared anatase TiO_2/graphene hybrid NSs with the fast lithium storage through a two-step method with the addition of organic additive.[8] The lithium diffusion was facilitated in TiO_2 NSs with (001) high energy faces, which leads to the excellent cyclic capacity retention and superior high-rate performance. Peng et al. prepared CuO NSs/graphene paper and investigated its lithium-storage performance.[9] As a binder-free anode material, the as-formed composite can deliver a capacity of 736.8 mAh g^{-1} after 50 cycles. Mitlin's group created electrodes consisting of MnO NPs anchored by graphene-like carbon sheets via hydrothermal carbonizing and activation of carbon sheets along with the deposition of MnO-precursor.[10] The resultant material exhibited good cyclic stability and high rate capacity.

Nowadays, the ever-growing market penetration of electric vehicles and hybrid electric vehicle requires the improvement of energy power, densities, and cycle endurance of electrode materials in LIBs.[11−15] As attractive candidate anode materials for LIBs, MnO-based materials have received tremendous research interest because of their appealing properties including low conversion potential and voltage hysteresis (<0.8 V) coupled with high theoretical capacity (756 mAh g^{-1}).[13−18] Besides, the natural abundance and the environmentally friendly characterization also promote the development of

Received: March 11, 2015
Accepted: May 22, 2015
Published: May 22, 2015

DOI: 10.1021/acsami.5b02171
ACS Appl. Mater. Interfaces 2015, 7, 12840−12849

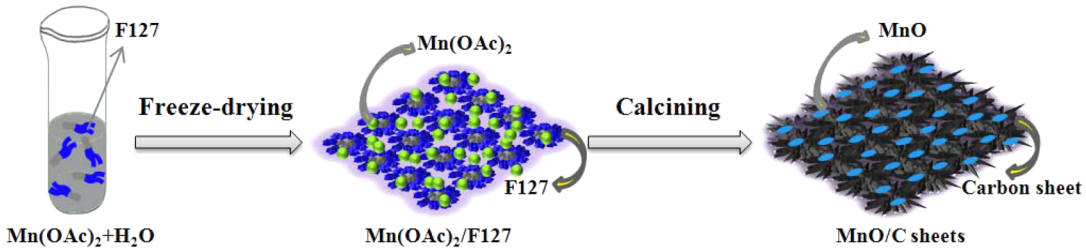

Figure 1. Schematic illustration of the fabrication process of the MnO/C hybrid.

MnO-based materials in LIBs. However, the inferior electrical conductivity and the severe volume change during the cycling process limit the enhancement of electrochemical performance and prevent the subsequent widespread applications.[19−21] Generally speaking, the former results in the poor rate capability, whereas the latter often leads to the disintegration of the electrode and subsequent electrical disconnection from the current collector.[22−24] Consequently, only if these two aspects are fully taken into consideration, the outstanding performance of MnO-based electrodes can be expected to be achieved.

Herein, we demonstrate a facile strategy for anchoring MnO NSs onto carbon sheets to form MnO/C hybrid via freeze-drying followed by thermal treatment under a N_2 atmosphere. Compared to the previous methods on the synthesis of NSs-based materials,[25−27] the current approach avoids the usage of templates, which is more efficient and time-saving. When used as an anode in LIBs, the resultant MnO/C hybrid shows distinct features: (1) an effective conductive pathway of carbon sheets interconnecting active materials can significantly improve charge transfer efficiency; (2) the firmly anchoring of MnO NSs on carbon sheets can not only effectively prevent the aggregation of MnO NSs, but also greatly alleviate the formation of unstable solid electrolyte interphase (SEI) layer upon repetitive volume changes and chemical interaction between electrolyte and electrode; (3) small-sized MnO NSs can efficiently mitigate the volume changes during discharge−charge processes. In view of these advantages, the resultant MnO/C hybrid displays high initial Coulombic efficiency, long-term cyclability and excellent rate capability when served as an anode material. Even at a high current density of 5 A g^{-1}, a capacity up to 1467.0 mA g^{-1} can still be achieved after 2000 cycles. Interesting, it was found that there exists a reconstruction for the MnO NSs with the electrochemical reaction. Specifically, the MnO NSs have transformed into ultrafine MnO NPs after repeated discharge−charge processes, which display better dispersion in the carbon sheets. These MnO NPs can introduce more electrochemically active sites, which also contribute greatly to the impressive electrochemical performance of the MnO/C hybrid electrode. To the best of our knowledge, this research may be represent the best performance reported so far for MnO-based materials.

2. EXPERIMENTAL SECTION

Synthesis of MnO/C NSs. In a typical synthetic procedure, 0.3 g of $Mn(OAc)_2{\cdot}4H_2O$ was dissolved into 15 mL of deionized water. Then, 0.5 g of Pluronic F127 was added. The resultant mixture was magnetically stirred to obtain a homogeneous solution. After 30 min, the solution was treated with liquid nitrogen rapidly and further freeze-dried for 24 h at −50 °C with a pressure of 20 Pa. Finally, the obtained loose precursor was calcined at 700 °C for 3 h under N_2 atmosphere with a heating rate of 3 °C min^{-1} to yield the target product (the typical MnO/C sample). For comparison, pure MnO and other MnO/C hybrids with different carbon contents were prepared by adjusting the usage of F127 (0.0, 0.3, 1.0, and 1.5 g) while keeping other conditions constant, and pure carbon was prepared by directly carbonizing freeze-dried F127.

Characterization. The field emission scanning electron microscopy (FE-SEM) was used to investigate the surface morphology by a JEOL S-4800 SEM unit. The transmission electron microscopy (TEM) and the energy-dispersive spectroscopic spectrum (EDS) element mapping of the sample were recorded using a JEOL 2010F microscope operated at 200 kV. The powder X-ray diffraction (XRD) measurements were performed on a Bruker D8 X-ray power diffractometer with the voltage of 40 kV and the current of 40 mA. Moreover, the cycled electrode materials were characterized by XRD and TEM techniques. Before testing, the electrodes obtained by disassembling the cells were washed by dimethyl carbonate (DEC) and then dried at the vacuum condition. Raman data were collected by using an Invia Raman spectrometer (633 nm laser for excitation). X-ray photoelectron spectra (XPS) were recorded by applying ESCALAB 250 spectrometer (PerkinElmer) to characterize the surface composition. The carbon contents of the as-resultant samples were calculated by an elemental analyzer (Vario EI) and a thermogravimetric (TG) instrument (DTG-60AH, from 25 to 700 °C with a heating rate of 10° min^{-1}). The freeze-drying was completed by a Freeze Drier (FD-1C-50).

Electrochemical Measurements. For the preparation of electrode, the active material, sodium carboxymethyl cellulose binder (CMC), conductive additive acetylene black were mixed with a weight ratio of 8:1:1 and ball-milled for 30 min. The mixture was then further milled into homogeneous slurry using deionized water as the solvent. The as-formed slurry was casting onto Cu foil uniformly and dried in a vacuum oven at 120 °C for 36 h. The mass loading of the active material was around 1.12 mg. Lithium foil was used as both counter electrode and reference electrode; a 1 M solution of $LiPF_6$ in ethylene carbonate (EC)/dimethyl carbonate (DMC)/diethyl carbonate (DEC) (1:1:1, vol %) was served as an electrolyte. Coin-type cells (CR2025) were assembled within an argon-filled glovebox. Before the electrochemically measurement, the prepared cells were aged in the glovebox for 24 h to make the electrode fully infiltrated by the electrolyte. Cyclic voltammetry (CV) measurement was carried out on a CHI-760E electrochemical workstation at a scanning rate of 0.1 mV s^{-1} with a potential window between 0.01 and 3 V. The impendence spectra were acquired by applying a sine wave with amplitude of 5 mV over the frequency range from 100 kHz to 0.01 Hz. The capacity of the MnO/C hybrid electrode is calculated on the basis of the total mass of MnO and carbon.

3. RESULT AND DISCUSSION

The preparation process of the MnO/C hybrid is schematically illustrated in Figure 1, which involves the freeze-drying, the carbonization of Pluronic F127 and the in situ formation of MnO NSs in N_2 atmosphere. Briefly, a transparent solution is first obtained after complete dissolution of $Mn(OAc)_2$ in deionized water. After the addition of Pluronic F127 into the above solution, the as-formed viscous mixture was fully mixed by violently stirring. During this process, the $Mn(OAc)_2$

DOI: 10.1021/acsami.5b02171
ACS Appl. Mater. Interfaces 2015, 7, 12840−12849

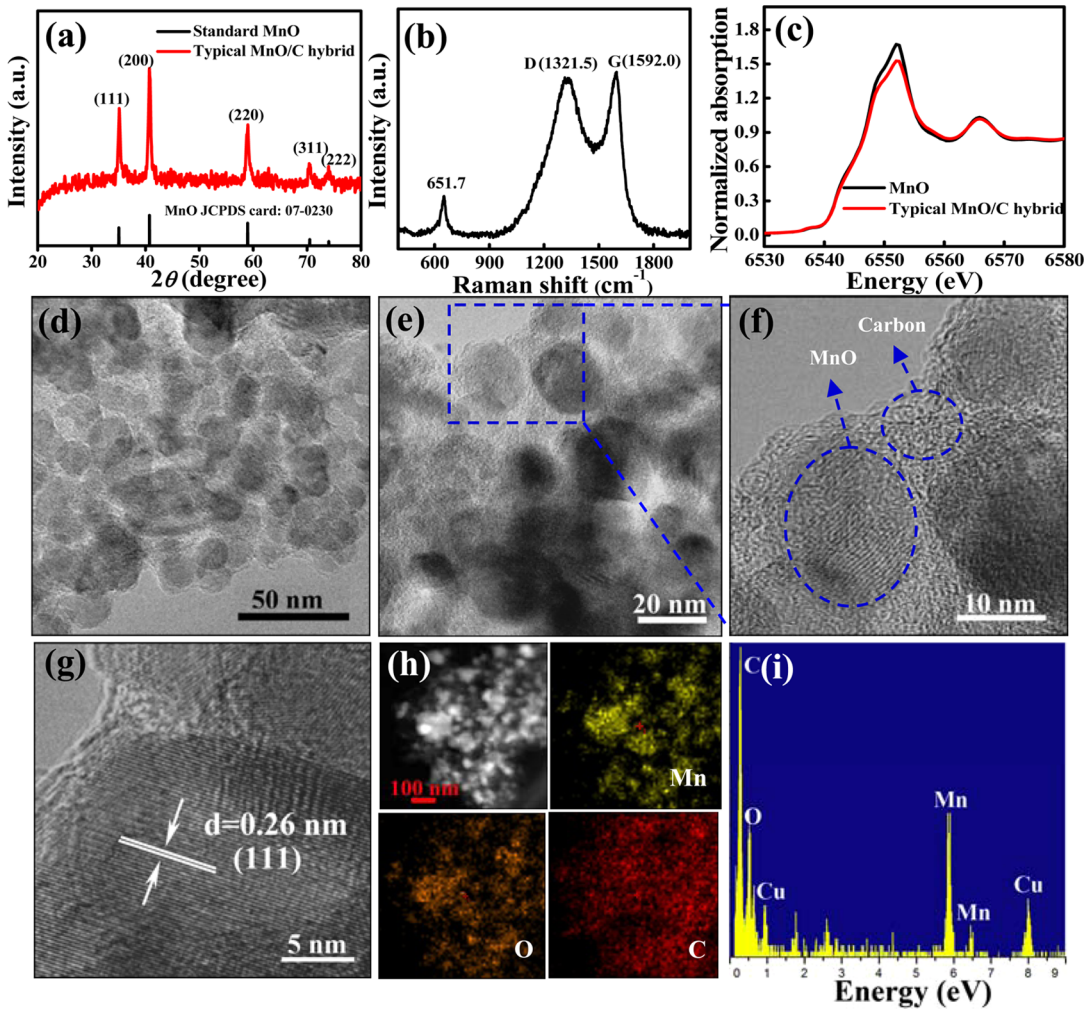

Figure 2. (a) XRD pattern and (b) Raman spectrum of the typical MnO/C hybrid. (c) XANES spectra of the typical MnO/C hybrid and pure MnO. (d–f) TEM images and (g) HRTEM image of the typical MnO/C hybrid. (h) STEM image and the element mapping images of Mn, O, and C. (i) EDS spectrum of the typical MnO/C hybrid.

molecules may be well-dispersed among the assembled Pluronic F127 molecules; the hydrogen bonds between Pluronic F127 and the surrounding water molecules could be beneficial for stabilizing the viscous solution. Then the as-obtained homogeneous and transparent solution was immersed into liquid nitrogen immediately and then treated with further freeze-drying. Finally, the freeze-dried sample was calcined in a continuous flux of N_2. During this process, Pluronic F127 was carbonized into carbon sheets along with the in situ decomposition of $Mn(OAc)_2$ into MnO phase. Here, it should be noted that the sheet morphology of the resultant carbon may result from the effective cross-linking effect among the dispersed Pluronic F127 molecules under the driving force of hydrogen bonding in water.[28−31] The freeze-drying process introduced in our experiments can prevent the reaggregation of F127 micelles, and thus the cross-linked structure between F127 monomers was maintained effectively, which may contribute to the final sheet morphology (Figure S1, Supporting Information). Then, the cross-linked F127 with well-dispersed structure was in stiu carbonizated into carbon sheets at a high temperature of 700 °C under a N_2 atmosphere. If the freeze-drying process was not used, the carbon obtained directly from the carbonizing of F127 exhibits an irregular bulk morphology with rare sheets (Figure S1, Supporting Information). As for the formation of carbon-anchored MnO nanosheets, the possible reason may be that the Mn-based salts can be well-dispersed in the cross-linked F127 micelles during the freeze-drying process, which will confine the decomposition of $Mn(OAc)_2$ to form MnO nanosheets. The carbon contents of MnO/C hybrids obtained with 0.3, 0.5, 1.0, and 1.5 g of Pluronic F127 determined from thermo-gravimetry (TG) analysis (Figure S2, Supporting Information) are 15.1, 24.8, 38.2, and 50.0%, respectively. The resultant MnO/C-24.8% sample was defined as the typical MnO/C hybrid and we use this sample as an example to detailedly investigate its composition and structure below.

The composition of the product was first characterized by X-ray diffraction (XRD) and Raman spectroscopy. The typical XRD pattern shown in Figure 2a suggests that the diffraction peaks located at about 35.1, 40.5, 58.7, 70.3, and 73.8° can be indexed as (111), (200), (220), (311), and (222) reflections of cubic MnO (JCPDS No: 07−0230). No other diffraction peaks belonging to impurities can be detected, indicating the effective formation of pure MnO through the current method. Raman spectroscopy further confirmed the formation of MnO and carbon in the resultant sample (Figure 2b). Specifically, the peak observed at 651.7 cm^{-1} can be ascribed to the Mn−O vibration according to the literature.[32] The other two obvious

DOI: 10.1021/acsami.5b02171
ACS Appl. Mater. Interfaces 2015, 7, 12840−12849

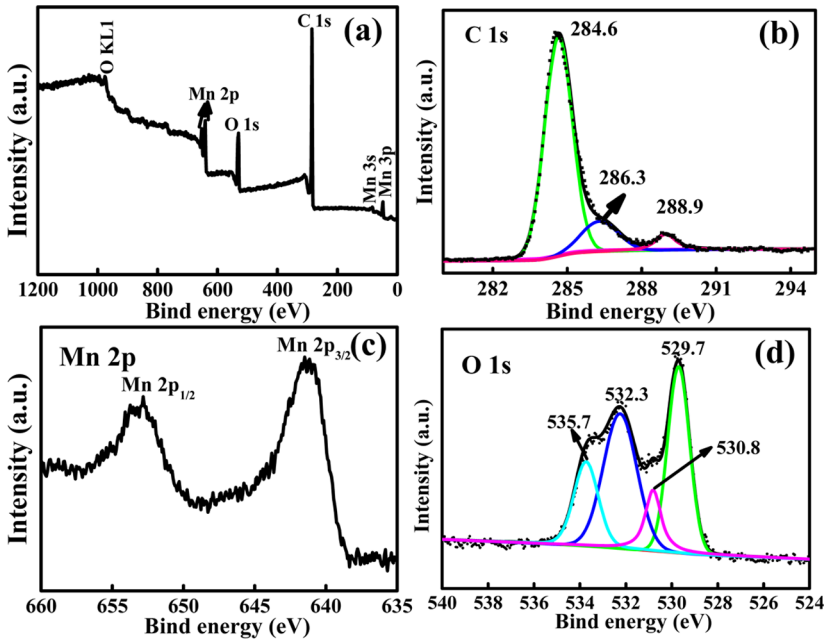

Figure 3. (a) Survey XPS spectrum, (b) C 1s high-resolution spectrum, (c) Mn 2p high-resolution spectrum, and (d) O 1s high-resolution spectrum of the typical MnO/C hybrid (the fitted curves are marked with color lines).

peaks at 1321.5 and 1592.0 cm^{-1} can be ascribed to typical D and G bands of carbon, respectively.[33−36] Besides, to further understand the interaction between MnO and carbon, we applied the X-ray absorption near-edge structure (XANES) spectrum to investigate the electronic structure of the typical MnO/C hybrid (Figure 2c). Compared to that of pure MnO sample, the Mn K-edge XANES spectrum of the typical MnO/C hybrid exhibits a decreased peak intensity at the Mn site, confirming the existence of interaction between the MnO and carbon.[24] This interaction will be beneficial for the well-anchoring of MnO NSs on the carbon sheets, thus exerting positive effect on its electrochemical performance.

The representative transmission electron microscopy (TEM) image displayed in Figure 2d indicates that the typical hybrid has sheet/sheet morphology and no single sheet was detected beyond the carbon layers. However, from field-emission scanning electron microscopy (FE-SEM) image (Figure S3, Supporting Information), we only observed a general sheet mophology of typical MnO/C hybrid. The magnified TEM image indicates that the MnO NSs present circle-like shape with an average diameter of about 20 nm. More importantly, Figure 2e, f shows that the MnO NSs were firmly embedded in the carbon sheets, which will be particularly beneficial for their lithium storage performance. Specifically, the firm connection between small-sized MnO and carbon sheet not only reduces the migration and aggregation of MnO and maintains more active sites,[24,30] but also leads to good electrical connection between them, both of which would have positive effects on electrochemical performance of MnO/C hybrid.[37] In addition, the firm connection can also alleviate the volume change during cycling and facilitate the stabilization of SEI film on the MnO surface.[13,17,35,37] In a word, the firm connection between MnO and carbon layer will be beneficial for the related electrochemical performance. High-resolution transmission electron microscopy (HRTEM) reveals the lattice fringe with interplanar spacing of 0.26 nm, which can be assigned to the (111) plane of cubic MnO phase (Figure 2g). Furthermore, the EDS spectrum confirms the presence of Mn, O, and C elements. Their scanning transmission electron microscopy (STEM) images (Figure 2h) clearly show the distribution of these three elements, which is in good agreement with the result from the TEM images.

Additionally, X-ray photoelectron spectroscopy (XPS) was further employed to give more insight into the chemical composition of the as-synthesized typical MnO/C hybrid. As shown in Figure 3a, in the survey spectrum, the detected peaks of Mn 2p, Mn 3s, Mn 3p, O 1s, O KLL, and C 1s indicates the presence of Mn, O, and C in the sample. The C 1s XPS spectrum (Figure 3b) can be resolved into three peaks at ca. 284.6, 286.3, and 288.9 eV, which correspond to sp^3C-sp^3C, C−O−C, and C−O, respectively.[14,38] The Mn 2p high-resolution spectrum (Figure 3c) shows two obvious signals at ca. 641.8 and 653.8 eV with a spin-energy separation of 12.0 eV, which can be attributed to the Mn $2p_{3/2}$ and Mn $2p_{1/2}$, respectively, confirming the formation of MnO.[14,39,40] The O 1s high-resolution spectrum shown in Figure 3c is fitted into four peaks at ca. 529.7, 530.8, 532.3, and 535.7 eV, corresponding to Mn−O, −OH, C−O−C, and C−O, respectively.[40] These results indicate the successful transformation of Mn^{2+}/F127 into MnO/C hybrid.

In view of superior structure feature, we tested the electrochemical performance of the resultant MnO/C hybrids in a half-cell configuration versus Li metal. The specific capacity is calculated on the basis of the whole sample (MnO and C). The cyclic voltammograms (CVs) of the typical MnO/C electrode for the first three cycles are shown in Figure 4a. In the first cycle, the reduction peak at ca. 0.10−0.20 V is observed, corresponding to the complete reduction of Mn^{2+} to Mn^0; the peaks at 0.63 and 1.25 V can be assigned to the irreversible reactions between Li and MnO accompanying with the formation of SEI layer.[17,18,41] From the second cycle, the reduction peak at 0.10−0.20 V shifts to ca. 0.38 V, which can be ascribed to the formation of Li_2O and metallic Mn.[14] In the anodic process, an obvious peak at ca. 1.32 V is observed, which

DOI: 10.1021/acsami.5b02171
ACS Appl. Mater. Interfaces 2015, 7, 12840−12849

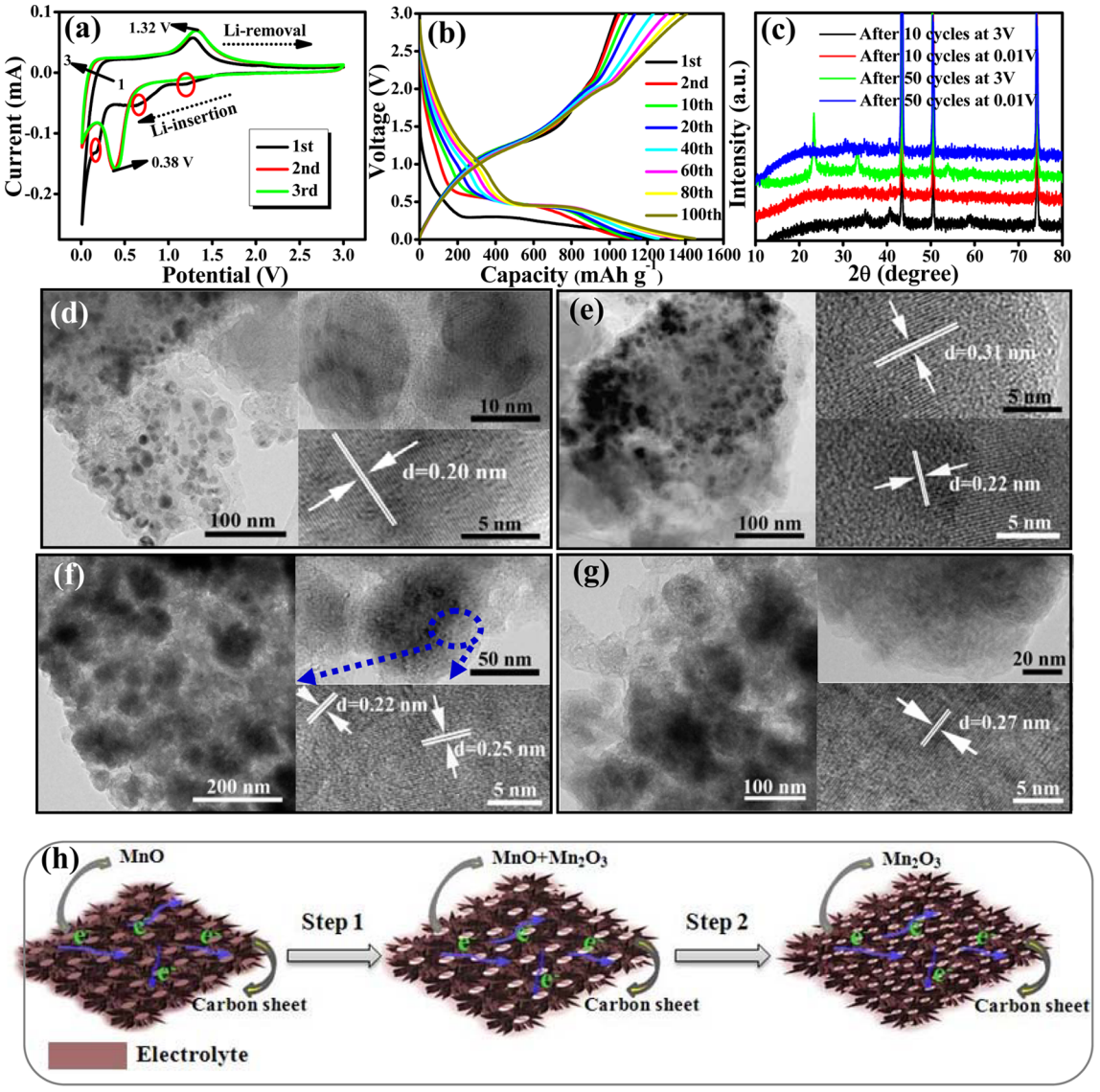

Figure 4. (a) CV curves and (b) discharge/charge profiles of the typical MnO/C electrode. (c) XRD patterns and (d–g) TEM images along with the corresponding HRTEM images of the typical MnO/C electrode after cycling. (d, e) represent the ones after 10 cycles at 0.01 and 3 V, respectively; (f, g) represent the ones after 50 cycles at 0.01 and 3 V, respectively.) (h) Schematic illustration of discharge–charge mechanism for the MnO/C electrode (the charged state is selected for the schematic picture).

should correspond to the oxidation of Mn^0 to Mn^{2+}. Both the reduction and oxidation curves almost overlap with the subsequent cycles from the second cycle, indicating excellent electrochemical reversibility of the typical MnO/C electrode. Galvanostatic measurements of the discharge–charge cycles are performed on the typical MnO/C electrode at 0.3 A g^{-1}, where several representative cycles (first, second, 10th, 20th, 40th, 60th, 80th, and 100th) are displayed (Figure 4b). A long voltage plateau at ca. 0.45 V in the discharge process and an obvious plateau at 1.20–2.00 V in the charge process before 10 cycles are clearly observed, matching well with the CV analysis. After 10 cycles, a charge slope at ca. 2.10 V oxidation curves almost overlap with the subsequent cycles from the second cycle, indicating along with a discharge slope at ca. 1.0 V appear and gradually broaden, and meanwhile, the previous long discharge plateau shifts to lower voltage (ca. 0.4 V), which are consistent with those of manganese oxides with higher oxidation states,[14] indicating an ever-increasing capacity and Li^+ reactivity.[14,42] XRD measurement was also used to understand the transformation process of the typical MnO/C electrode during the discharge–charge process. As shown in Figure 4c, when the cell was discharged to 0.01 V after 10 and 50 cycles, respectively, the electrochemical reaction results in the formation of metal Mn, whereas in the corresponding charged state, the MnO phase can be regenerated after 10 cycles. However, the XRD analysis of the electrode after 50 cycles indicated the formation of pure Mn_2O_3, suggesting the enhanced kinetics of conversion reactions upon cycling. This result is in agreement with the galvanostatic analysis.

To further understand and confirm the electrochemical mechanism of the MnO/C hybrid, we investigated the electrode after different cycles at different states by TEM measurements. As displayed in Figure 4d, e, the electrode after 10 cycles still shows a morphology similar to that of original typical MnO/C hybrid. Its lattice spacings of 0.20, 0.22, and 0.31 nm in the HRTEM images further confirm the formation of metal Mn and MnO complying with Mn_2O_3 at discharged and charged states, respectively. However, after 50 cycles

DOI: 10.1021/acsami.5b02171
ACS Appl. Mater. Interfaces 2015, 7, 12840–12849

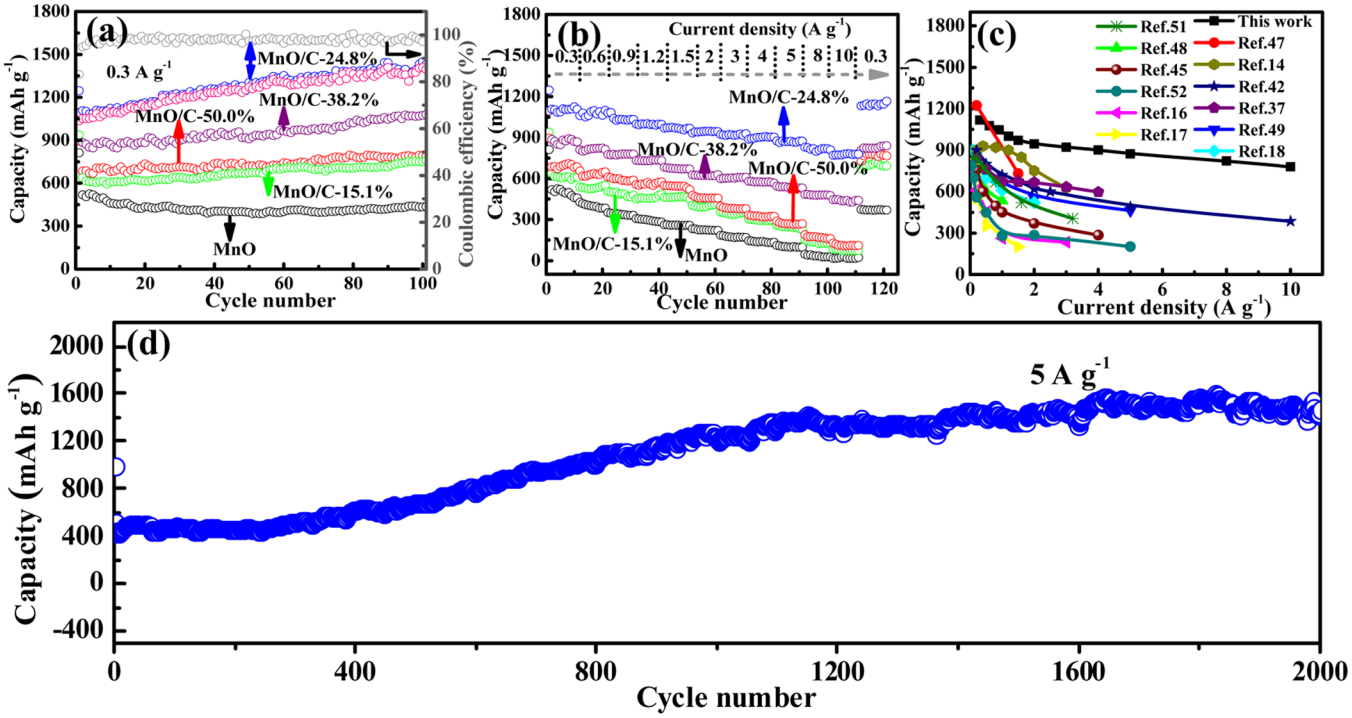

Figure 5. (a) Cycling performance of the MnO/C electrodes obtained with different carbon contents at 0.3 A g^{-1} along with the Coulombic efficiency of typical MnO/C electrode. (b) Comparison of rate performance of the typical MnO/C electrode with control samples at various current densities. (c) Rate capability comparison of this work with previously reported MnO-based anodes. (d) Cycling performance of the typical MnO/C hybrid at 5 A g^{-1} for 2000 cycles.

(Figure 4f, g), the electrode almost maintains the original morphology of MnO/C. The products on carbon sheets become larger and are composed of small NPs. HRTEM images reveal well-dispersed nanocrystallites with the lattice fringes of 0.22 and 0.25 nm for the electrode at discharged state, complying with the value of 0.27 nm at the charged state, suggesting the existence of Mn as a discharged product and Mn_2O_3 as a charged product after 50 cycles. Such a uniform distribution of NPs in the product is favorable for the electrochemical activation of the materials, leading to its enhanced electrochemical performance as an anode.[43,44] The corresponding electrochemical process can be clearly expressed in Figure 4h.

Furthermore, we also investigated the effect of the carbon content on the lithium storage of MnO/C hybrid. The MnO/C hybrids obtained with 0.3, 0.5, 1.0, and 1.5 g of Pluronic F127 were successively denoted as MnO/C-15.1%, MnO/C-24.8%, MnO/C-38.2%, MnO/C-50.0%. (The related characterization for MnO/C-15.1%, MnO/C-38.2% and MnO/C-50.0% were displayed in Figure S4, Supporting Information). Figure 5a displays the cycling performance of MnO/C samples with different carbon contents. It can be seen that the typical MnO/C hybrid (MnO/C-24.8%) delivers a specific capacity as high as 1449.8 mAh g^{-1} after 100 cycles, which is far higher than 1080.6 mAh g^{-1} for MnO/C-38.2%, 792.9 mAh g^{-1} for MnO/C-50.0%, and 749.6 mAh g^{-1} for MnO/C-15.1%. On the contrary, bare MnO exhibits very poor lithium storage performance and only 433.9 mAh g^{-1} of specific capacity can be obtained. Similarly, pure carbon also displays a low capacityer of ca. 220.1 mAh g^{-1} (Figure S5, Supporting Information). Clearly, the MnO/C-24.8% hybrid shows the best performance among all the samples, indicating the important role of carbon content in improving the lithium storage of MnO. Meanwhile, the initial Coulombic efficiency of the MnO/C-24.8% sample is up to 83.1% and this value can rapidly reach above 98.0% after the first two cycles, which is significant for its practical application. The fact that the reversible capacity increases with the proceeding of cycling may result from the progressive formation of electrochemistry active polymeric gel-like films, the interfacial Li storage, or the generation of LiOH and its sunsquent reversible reation with Li to form Li_2O and LiH.[13,17,45−47] The rate performance of the samples was performed by the stepwise increase with each step consisting of 10 discharge−charge cycles from 0.3 to 10 A g^{-1}, and then returning to 0.3 A g^{-1} (Figure 5b and Figure S5 in the Supporting Information). The MnO/C-24.8% hybrid displays the best performance and delivers final discharge capacities of 1123.7, 1098.2, 1032.2, 967.6, 928.1, 873.6, and 778.7 mAh g^{-1} at current densities of 0.3, 0.6, 0.9, 1.5, 3, 5, and 10 A g^{-1}, respectively. Figure S6 in the Supporting Information shows the corresponding diacharge−charge profiles. When the current density was brought back to 0.3 A g^{-1}, the discharge capacity reaches a value of 1165.4 mAh g^{-1} in spite of the cycling at high current densities, which is close to the capacity of the first 10 cycles at this current density, indicating an outstanding rate performance. This rate performance of the MnO/C-24.8% hybrid is far better than those of previously reported high efficient MnO-based materials (Figure 5c).[14,16−18,37,42,45,47−52] As well-known, the long-term performance and good capability at high rates play a significant role in electric vehicle and hybrid vehicle. Therefore, we also tested a long-term cycling performance of the MnO/C-24.8% hybrid at a current density of 5 A g^{-1} for 2000 cycles, and a reversible capacity as high as 1467.0 mAh g^{-1} can be retained after 2000 cycles. Obviously, the capacity keeps relatively steady in the first 250 cycles and subsequently, there is a gradual increase in the capacity in the

DOI: 10.1021/acsami.5b02171
ACS Appl. Mater. Interfaces 2015, 7, 12840−12849

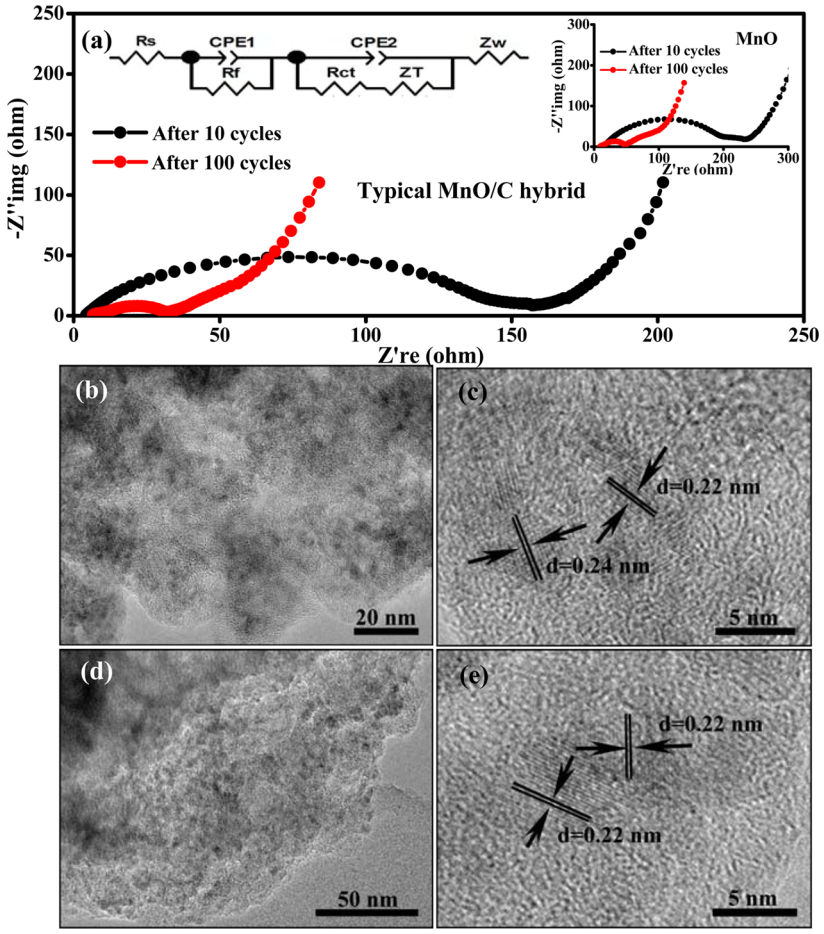

Figure 6. (a) Nyquist plots of the typical MnO/C hybrid and bare MnO (the right inset) after different cycles at 0.3 A g^{-1}. The left inset is the corresponding equivalent circuit model. TEM images of the MnO/C electrode: (b, c) after 100 cycles at 0.3 A g^{-1}; (d, e) after 2000 cycles at 5 A g^{-1}.

following cyles up to 1000 cycles. On the basis of the related literatures,[13,17,53−58] this phenomenon could be reasonably explained by following several aspects. First, the progressive formation of electrochemistry active gel-like film resulting from the kinetically active electrolyte degradation, can prevent the aggregation of active materials and alleviate the volumetric variation on cycling.[53−55] Second, more active materials in carbon sheets may transform into small size nanograins upon cycling, which can increase the specific surface to some extent, thus leading to the enhancement of the interfacial Li storage ability and the increase of capacity.[13,17,53] Third, the presence of Li_2O formed during the electrochemical process can not only effectively restrain the aggregation of active materials, leading to the retaining of the surface area, but also enhance the capacity related to the gel-like film.[13,56,57] Additionally, Li_2O can act as an oxidant to make the metal valence transform into higher states and thus there exists a dynamic enhanced process during cycling, which can partially lead to the increase in the capacity.[56,57] Finally, the as-formed metal nanograins can catalyze the formation and dissolution of the electrolyte, enhancing the reversible ability of electrochemical reaction and leading to more "extra capacities".[13,55,58] The cycling capacity and stability of the MnO/C-24.8% (the typical MnO/C hybrid) electrode were also far superior to those of the MnO-based anodes in the literatures (Table S1, Supporting Information).

To further understand the effect of carbon compositing on the resulted electrode, we performed electrochemical impedance spectroscopy (EIS) measurement of the typical MnO/C and bare MnO electrodes. Figure 6a shows Nyquist plots of the typical MnO electrode after 10 and 100 cycles. The inset one in the left part displays the equivalent circuit of the impedance results. That in the right part displays the Nyquist plots of the MnO electrode after different cycles. As can be seen, these Nyquist plots have similar features. The high-frequency region of the semicircle represents the SEI resistance (R_{SEI}) and contact resistance (R_f), and the high-medium frequency region represents the charge transfer resistance (R_{ct}) on the electrode/electrolyte interface, whereas the parts after the semicircle at low frequency correspond to diffusion barrier layer impedance (Z_T) and semi-infinite diffusion impedance (Z_w), respectively.[59−62] From Figure 6a, it can be observed that the semicircle diameter in the high-media-frequency region for the typical MnO/C electrode after 100 cycles is significantly smaller than that of the same electrode after 10 cycles, suggesting a decreased cell impedance with ongoing cycling. Furthermore, compared with that of the bare MnO (inset one), the smaller impedance of the MnO/C electrode in the high-media-frequency region after 100 cycles, illustrates its superior rate performance as well as the important effect of carbon incorporation on increasing the electrical conductivity and reducing the charge-transfer impedance. This conclusion is in well consistent with the fitted results based on the equivalent circuit. According to the fitted results, the typical MnO/C gives charge transfer resistances (R_{ct}) of 140 and 13.3 Ω after 10 and 100 cycles, much smaller than those of the pure MnO (192.3 and 51.6 Ω), exhibiting a decreased charge transfer resistances

DOI: 10.1021/acsami.5b02171
ACS Appl. Mater. Interfaces 2015, 7, 12840−12849

after carbon hybridization. Besides, the SEI resistances (R_{SEI}) of the typical MnO/C electrode are calculated to be 9.5 and 9.4 Ω after 10 and 100 cycles, respectively. Meanwhile, bare MnO presents lower values of 27.2 and 19.3 Ω. The slighter change in R_{SEI} for the former implies that the typical MnO/C electrode has a more stabilized SEI layer, which was believed to be ascribed to carbon hybridization in the electrode.[16,34,63]

To disclose the morphology of typical MnO/C electrode after cycling, we applied TEM analysis (Figure 6b−e). Both of the electrode materials after 100 cycles with a discharged state at 0.3 A g^{-1} and 2000 cycles at 5 A g^{-1} display similar morphology, which almost preserved the overall shape. However, the original sheet/sheet morphology was transformed into ultrafine particles/C sheets. Even after 2000 cycles at high current density (5 A g^{-1}), small NPs can still homogeneously disperse on the carbon matrix without obvious aggregation, suggesting the excellent structural stability of the current restructured electrode. HRTEM images indicate the formation of Mn particles (lattice fringes with an interplanar distance of 0.24 and 0.22 nm) during the lithiation process. The homogeneous distribution of small NPs may make them connect electrochemically with the carbon more closely and benefit for the charge transfer; meanwhile, the smaller size of the NPs will partially alleviate the volume changes and significantly reduce the Li^+ transport path, all of which contributed to the final excellent electrochemical performance.[13,14,20]

On the basis of the above analysis, the excellent performance of the current electrode material can be attributed to the following several aspects. First, the presence of carbon can not only enhance the electrode's conductivity and stabilize the stability of SEI film on the surface of electrode, but also relieve the volume changes during the cycling effectively.[34,63] Second, the close connection between MnO and C can reduce the aggregation of MnO NPs and generate more active sites.[24,35] Third, MnO with small size will induce abundant active sites, reduce the transfer path of Li^+, and mitigate the pulverization of the electrode material. All of these aspects contribute to the long-term cycling ability and excellent rate capability of the MnO/C hybrid.

4. CONCLUSION

In summary, a facile integration of carbon sheets with MnO NSs was reported as an effective strategy to significantly improve electrochemical performance of MnO. The as-formed MnO/C hybrid presents excellent Li storage properties and outstanding rate capability. On the one hand, the highly electrical conductive carbon sheets can not only stabilize the MnO NSs against self-agglomeration and provide a conductive channel to improve the charge transfer efficiency but also alleviate the formation of unstable SEI upon repetitive volume changes during cycling. On the other hand, the carbon sheets can effectively buffer the volume changes of MnO during the electrochemical reaction process. The superior cyclability and rate performance of the as-formed MnO/C hybrid can be attributed to the synergistic effects of carbon component and good reconstruction of the MnO NSs during cycling. The high-rate and long-term cycling properties demonstrated that the current material is highly promising in high-power LIBs.

■ ASSOCIATED CONTENT

Supporting Information

Photographs of commercial F127 and freeze-dried F127, and TEM and FE-SEM images of the carbonized product; TG curves of all the samples performed at air atmosphere; SEM image of the typical MnO/C hybrid; characterization of the control samples including XRD patterns, Raman spectra, TEM images; discharge−charge profiles of the typical sample at different current densities; cycling performance and rate capability of pure carbon; table of cycling performance comparison of the current material with previous reported MnO-based materials. This material is available free of charge via the Internet at http://pubs.acs.org/.The Supporting Information is available free of charge on the ACS Publications website at DOI: 10.1021/acsami.5b02171.

■ AUTHOR INFORMATION

Corresponding Author

*E-mail: caomh@bit.edu.cn. Fax: +86-10-68918572. Tel: +86-10-68918468.

Notes

The authors declare no competing financial interest.

■ ACKNOWLEDGMENTS

This work was financially supported by the National Natural Science Foundation of China (21471016 and 21271023) and the 111 Project (B07012).

■ REFERENCES

(1) Niu, C. J.; Meng, J. S.; Han, C. H.; Zhao, K. N.; Yan, M. Y.; Mai, L. Q. VO_2 Nanowires Assembled into Hollow Microspheres for High-Rate and Long-Life Lithium Batteries. *Nano Lett.* **2014**, *14*, 2873−2878.

(2) Chen, C. J.; Hu, P.; Hu, X. L.; Mei, Y. N.; Huang, Y. H. Bismuth Oxyiodide Nanosheets: A Novel High-Energy Anode Mater for Lithium-Ion Batteries. *Chem. Commun.* **2015**, *51*, 2798−2801.

(3) Jiang, J.; Li, Y. Y.; Liu, J. P.; Huang, X. T.; Yuan, C. Z.; Lou, X. W. Recent Advances in Metal Oxide-based Electrode Architecture Design for Electrochemical Energy Storage. *Adv. Mater.* **2012**, *24*, 5166−5180.

(4) Cao, A. M.; Hu, J. S.; Liang, H. P.; Wan, L. J. Self-Assembled Vanadium Pentoxide (V_2O_5) Hollow Microspheres from Nanorods and Their Application in Lithium-Ion Batteries. *Angew. Chem., Int. Ed.* **2005**, *44*, 4391−4395.

(5) Geim, A. K.; Novoselov, K. S. The Rise of Grapheme. *Nat. Mater.* **2007**, *6*, 183−191.

(6) Deng, J. W.; Yan, C. L.; Yang, L. C.; Baunack, S.; Oswald, S.; Wendrock, H.; Mei, Y. F.; Schmidt, O. G. Sandwich-Stacked SnO_2/Cu Hybrid Nanosheets as Multichannel Anodes for Lithium Ion Batteries. *ACS Nano* **2013**, *7*, 6948−6954.

(7) Zhou, G. M.; Wang, D. W.; Yin, L. C.; Li, N.; Li, F.; Cheng, H. M. Oxygen Bridges between NiO Nanosheets and Graphene for Improvement of Lithium Storage. *ACS Nano* **2012**, *6*, 3214−3223.

(8) Chen, J. S.; Liu, H.; Qiao, S. Z.; Lou, X. W. Carbon-Supported Ultra-Thin Anatase TiO_2 Nanosheets for Fast Reversible Lithium Storage. *J. Mater. Chem.* **2011**, *21*, 5687−5692.

(9) Liu, Y.; Wang, W.; Gu, L.; Wang, Y. W.; Ying, Y. L.; Mao, Y. Y.; Sun, L. W.; Peng, X. S. Flexible CuO Nanosheets/Reduced-Graphene Oxide Hybrid Paper: Binder-Free Anode for High-Performance Lithium-Ion Batteries. *ACS Appl. Mater. Interfaces* **2013**, *5*, 9850−9855.

(10) Wang, H. L.; Xu, Z. W.; Li, Z.; Cui, K.; Ding, J.; Kohandehghan, A.; Tan, X. H.; Zahiri, B.; Olsen, B. C.; Holt, C. M. B.; Mitlin, D. Hybrid Device Employing Three-Dimensional Arrays of MnO in Carbon Nanosheets Bridges Battery−Supercapacitor Divide. *Nano Lett.* **2014**, *14*, 1987−1994.

DOI: 10.1021/acsami.5b02171
ACS Appl. Mater. Interfaces 2015, 7, 12840−12849

(11) Wen, W.; Wu, J. M. Eruption Combustion Synthesis of NiO/Ni Nanocomposites with Enhanced Properties for Dye-Absorption and Lithium Storage. *ACS Appl. Mater. Interfaces* **2011**, *3*, 4112−4119.
(12) Wang, S. B.; Xing, Y. L.; Xu, H. Z.; Zhang, S. C. MnO Nanoparticles Interdispersed in 3D Porous Carbon Framework for High Performance Lithium-Ion Batteries. *ACS Appl. Mater. Interfaces* **2014**, *6*, 12713−12718.
(13) Sun, Y. M.; Hu, X. L.; Luo, W.; Xia, F. F.; Huang, Y. H. Reconstruction of Conformal Nanoscale MnO on Graphene as a High-Capacity and Long-Life Anode Material for Lithium Ion Batteries. *Adv. Funct. Mater.* **2013**, *23*, 2436−2444.
(14) Xiao, Y.; Wang, X.; Wang, W.; Zhao, D.; Cao, M. H. Engineering Hybrid between MnO and N-Doped Carbon to Achieve Exceptionally High Capacity for Lithium-Ion Battery Anode. *ACS Appl. Mater. Interfaces* **2014**, *6*, 2051−2058.
(15) Su, H.; Xu, Y. F.; Feng, S. C.; Wu, Z. G.; Sun, X. P.; Shen, C. H.; Wang, J. Q.; Li, J. T.; Huang, L.; Sun, S. G. Hierarchical Mn_2O_3 Hollow Microspheres as Anode Material of Lithium Ion Battery and its Conversion Reaction Mechanism Investigated by XANES. *ACS Appl. Mater. Interfaces* **2015**, *7*, 8488−8494.
(16) Xia, Y.; Xiao, Z.; Dou, X.; Huang, H.; Lu, X. H.; Yan, R. J.; Gan, Y. P.; Zhu, W. J.; Tu, J. P.; Zhang, W. K.; Tao, X. Y. Green and Facile Fabrication of Hollow Porous MnO/C Microspheres from Microalgaes for Lithium-Ion Batteries. *ACS Nano* **2013**, *7*, 7083−7092.
(17) Liu, B.; Hu, X. L.; Xu, H. H.; Luo, W.; Sun, Y. M.; Huang, Y. H. Encapsulation of MnO Nanocrystals in Electrospun Carbon Nanofibers as High-Performance Anode Materials for Lithium-Ion Batteries. *Sci. Rep.* **2014**, *4*, 4229−4234.
(18) Wang, T. Y.; Peng, Z.; Wang, Y. H.; Tang, J.; Zheng, G. F. MnO Nanoparticle@Mesoporous Carbon Hybrids Grown on Conducting Substrates Featuring High-performance Lithium-ion Battery, Supercapacitor and Sensor. *Sci. Rep.* **2013**, *3*, 2693−2701.
(19) Yu, X. Q.; He, Y.; Sun, J. P.; Tang, K.; Li, H.; Chen, L. Q.; Huang, X. J. Nanocrystalline MnO Thin Film Anode for Lithium Ion Batteries with Low Overpotential. *Electrochem. Commun.* **2009**, *11*, 791−794.
(20) Zhong, K. F.; Xia, X.; Zhang, B.; Li, H.; Wang, Z. X.; Chen, L. Q. MnO Powder as Anode Active Materials for Lithium Ion Batteries. *J. Power Sources* **2010**, *195*, 3300−3308.
(21) Qiu, D. F.; Ma, L. Y.; Zheng, M. B.; Lin, Z. X.; Zhao, B.; Wen, Z.; Hu, Z. B.; Pu, L.; Shi, Y. MnO Nanoparticles Anchored on Graphene Nanosheets *via in Situ* Carbothermal Reduction as High-Performance Anode Materials for Lithium-Ion Batteries. *Mater. Lett.* **2012**, *84*, 9−12.
(22) Gu, M.; Li, Y.; Li, X.; Hu, S.; Zhang, X.; Xu, W.; Thevuthasan, S.; Baer, D. R.; Zhang, J. G.; Liu, J.; Wang, C. In Situ TEM Study of Lithiation Behavior of Silicon Nanoparticles Attached to and Embedded in a Carbon Matrix. *ACS Nano* **2012**, *6*, 8439−8447.
(23) Xiao, Y.; Cao, M. H. High-Performance Lithium Storage Achieved by Chemically Binding Germanium Nanoparticles with N-Doped Carbon. *ACS Appl. Mater. Interfaces* **2014**, *6*, 12922−12930.
(24) Zhou, X. S.; Wan, L. J.; Guo, Y. G. Binding SnO_2 Nanocrystals in Nitrogen-Doped Graphene Sheets as Anode Materials for Lithium-Ion Batteries. *Adv. Mater.* **2013**, *25*, 2152−2157.
(25) Son, J. S.; Wen, X. D.; Joo, J.; Chae, J.; Baek, S. l.; Park, K.; Kim, J. H.; An, K.; Yu, J. H.; Kwon, S. G.; Choi, S. H.; Wang, Z. W.; Kim, Y. W.; Kuk, Y.; Hoffmann, R.; Hyeon, T. Large-Scale Soft Colloidal Template Synthesis of 1.4 nm Thick CdSe Nanosheets. *Angew. Chem., Int. Ed.* **2008**, *48*, 6861−6864.
(26) Zhao, G. X.; Li, J. X.; Jiang, L.; Dong, H. L.; Wang, X. K.; Hu, W. P. Synthesizing MnO_2 Nanosheets from Graphene Oxide Templates for High Performance Pseudosupercapacitors. *Chem. Sci.* **2012**, *3*, 433−437.
(27) Xu, C.; Zeng, Y.; Rui, X. H.; Xiao, N.; Zhu, J. X.; Zhang, W. Y.; Chen, J.; Liu, W. L.; Tan, H. T.; Hug, H. H.; Yan, Q. Y. Controlled Soft-Template Synthesis of Ultrathin C@FeS Nanosheets with High-Li-Storage Performance. *ACS Nano* **2012**, *6*, 4713−4721.
(28) Meng, Y.; Gu, D.; Zhang, F. Q.; Shi, Y. F.; Yang, H. F.; Li, Z.; Yu, C. Z.; Tu, B.; Zhao, D. Y. Ordered Mesoporous Polymers and Homologous Carbon Frameworks: Amphiphilic Surfactant Templating and Direct Transformation. *Angew. Chem., Int. Ed.* **2005**, *44*, 7053−7059.
(29) Chen, K. Y.; Wan, C. Y.; Wei, W.; Huang, X. B.; Liu, H. Convenient One-Pot Approach for the Preparation of Novel Atomically Thin Two-Dimensional Polymeric Nanosheets, and Its Evolution in Aqueous Solution. *Mater. Lett.* **2015**, *139*, 93−97.
(30) Xiao, Y.; Zheng, L. R.; Cao, M. H. Hybridization and Pore Engineering for Achieving High-Performance Lithium Storage of Carbide as Anode Material. *Nano Energy* **2015**, *12*, 152−160.
(31) Xiao, Y.; Cao, M. H. Freeze-Drying-Assisted Synthesis of Hierarchically Porous Carbon/Germanium Hybrid for High-Efficiency Lithium-Ion Batteries. *Chem. − Asian J.* **2014**, *9*, 2859−2865.
(32) Liao, Q. Y.; Li, N.; Cui, H.; Wang, C. X. Vertically-Aligned Graphene@MnO Nanosheets as Binder-Free High-Performance Electrochemical Pseudocapacitor Electrodes. *J. Mater. Chem. A* **2013**, *1*, 13715−13720.
(33) Hu, C. G.; Wang, L. X.; Zhao, Y.; Ye, M. H.; Chen, Q.; Feng, Z. H.; Qu, L. T. Designing Nitrogen-Enriched Echinus-Like Carbon Capsules for Highly Efficient Oxygen Reduction Reaction and Lithium Ion Storage. *Nanoscale* **2014**, *6*, 8002−8009.
(34) Hu, C. G.; Zheng, G. P.; Zhao, F.; Shao, H. B.; Zhang, Z. P.; Chen, N.; Jiang, L.; Qu, L. T. A Powerful Approach to Functional Graphene Hybrids for High Performance Energy-Related Applications. *Energy Environ. Sci.* **2014**, *7*, 3699−3708.
(35) Xiao, Y.; Sun, P. P.; Cao, M. H. Core-Shell Bimetallic Carbide Nanoparticles Confined in a Three-Dimensional N-Doped Carbon Conductive Network for Efficient Lithium Storage. *ACS Nano* **2014**, *8*, 7846−7857.
(36) Gu, X.; Yue, J.; Chen, L.; Liu, S.; Xu, H. Y.; Yang, J.; Qian, Y. T.; Zhao, X. B. Coaxial MnO/N-Doped Carbon Nanorods for Advanced Lithium-Ion Battery Anodes. *J. Mater. Chem. A* **2015**, *3*, 1037−1041.
(37) Jiang, H.; Hu, Y. J.; Guo, S. J.; Yan, C. Y.; Lee, P. S.; Li, C. Z. Rational Design of MnO/Carbon Nanopeapods with Internal Void Space for High-Rate and Long-Life Li-Ion Batteries. *ACS Nano* **2014**, *8*, 6038−6046.
(38) Mao, Y.; Duan, H.; Xu, B.; Zhang, L.; Hu, Y. S.; Zhao, C. C.; Wang, Z. X.; Chen, L. Q.; Yang, Y. S. Lithium Storage in Nitrogen-Rich Mesoporous Carbons. *Energy Environ. Sci.* **2012**, *5*, 7950−7955.
(39) Dubal, D. P.; Dhawale, D. S.; Salunkhe, R. R.; Lokhande, C. D. A Novel Chemical Synthesis of Mn_3O_4 Thin Film and Its Stepwise Conversion into Birnessite MnO_2 during Super Capacitive Studies. *J. Electroanal. Chem.* **2010**, *647*, 60−65.
(40) Qiu, S.; Wang, X. Z.; Lu, G. X.; Liu, J. R.; He, C. Z. Facile Synthesis of MnO and Nitrogen-Doped Carbon Nanocomposites as Anode Material for Lithium Ion Battery. *Mater. Lett.* **2014**, *136*, 289−291.
(41) Li, X. W.; Li, D.; Qiao, L.; Wang, X. H.; Sun, X. L.; Wang, P.; He, D. Y. Interconnected Porous MnO Nanoflakes for High-Performance Lithium Ion Battery Anodes. *J. Mater. Chem.* **2012**, *22*, 9189−9194.
(42) Chen, W. M.; Qie, L.; Shen, Y.; Sun, Y. M.; Yuan, L. X.; Hu, X. L.; Zhang, W. X.; Huang, Y. H. Superior Lithium Storage Performance in Nanoscaled MnO Promoted by N-Doped Carbon Webs. *Nano Energy* **2013**, *2*, 412−418.
(43) Qian, J. F.; Xiong, Y.; Cao, Y. L.; Ai, X. P.; Yang, H. X. Synergistic Na-Storage Reactions in Sn_4P_3 as a High-Capacity, Cyclestable Anode of Na-Ion Batteries. *Nano Lett.* **2014**, *14*, 1865−1869.
(44) Zhang, S.; Zhu, L. X.; Song, H. J.; Chen, X. H.; Zhou, J. S. Enhanced Electrochemical Performance of MnO Nanowire/Graphene Composite during Cycling as the Anode Material for Lithium-Ion Batteries. *Nano Energy* **2014**, *10*, 172−180.
(45) Zhang, K. J.; Han, P. X.; Gu, L.; Zhang, L. X.; Liu, Z. H.; Kong, Q. S.; Zhang, C. J.; Dong, S. M.; Zhang, Z. Y.; Yao, J. H.; Xu, H. X.; Cui, G. L.; Chen, L. Q. Synthesis of Nitrogen-Doped MnO/Graphene Nanosheets Hybrid Material for Lithium Ion Batteries. *ACS Appl. Mater. Interfaces* **2014**, *4*, 658−664.

DOI: 10.1021/acsami.5b02171
ACS Appl. Mater. Interfaces 2015, 7, 12840−12849

(46) Grugeon, S.; Laruelle, S.; Dupont, L.; Tarascon, J. M. An Update on the Reactivity of Nanoparticles Co-Based Compounds towards Li. *Solid State Sci.* **2003**, *5*, 895−904.
(47) Hu, Y. Y.; Liu, Z. G.; Nam, K. W.; Borkiewicz, O. J.; Cheng, J.; Hua, X.; Dunstan, M. T.; Yu, X. Q.; Wiaderek, K. M.; Du, L. S.; Chapman, K. W.; Chupas, P. J.; Yang, X. Q.; Grey, C. P. Origin of Additional Capacities in Metal Oxide Lithium-Ion Battery Electrodes. *Nat. Mater.* **2013**, *12*, 1130−1136.
(48) Luo, W.; Hu, X. L.; Sun, Y. M.; Huang, Y. H. Controlled Synthesis of Mesoporous MnO/C Networks by Microwave Irradiation and Their Enhanced Lithium-Storage Properties. *ACS Appl. Mater. Interfaces* **2013**, *5*, 1997−2003.
(49) Sun, Y. M.; Hu, X. L.; Luo, W.; Huang, Y. H. Porous Carbon-Modified MnO Disks Prepared by a Microwave-Polyol Process and Their Superior Lithium-Ion Storage Properties. *J. Mater. Chem.* **2012**, *22*, 19190−19195.
(50) Wang, S. B.; Ren, Y. B.; Liu, G. R.; Xing, Y. L.; Zhang, S. C. Peanut-Like MnO@C Core−Shell Composites as Anode Electrodes for High-Performance Lithium Ion Batteries. *Nanoscale* **2014**, *6*, 3508−3512.
(51) Qiu, T.; Wang, J.; Lu, Y. L.; Yang, W. S. Facile Fabrication of Chinese Lantern-Like MnO@N−C: A High-Performance Anode Material for Lithium-Ion Batteries. *RSC Adv.* **2014**, *4*, 23027−23035.
(52) Su, K.; Wang, C.; Nie, H. G.; Guan, Y.; Liu, F.; Chen, J. T. Facile Template-Free Synthesis of 3D Porous MnO/C Microspheres with Controllable Pore Size for High Performance Lithium-Ion Battery Anodes. *J. Mater. Chem. A* **2014**, *2*, 10000−10006.
(53) Yu, Y.; Shi, Y.; Chen, C. H. Effect of Lithia and Substrate on the Electrochemical Performance of a Lithia/Cobalt Oxide Composite Thin-Film Anode. *Chem. − Asian J.* **2006**, *1*, 826−831.
(54) Yu, Y.; Chen, C. H.; Shi, Y. A Tin-Based Amorphous Oxide Composite with a Porous, Spherical, Multideck-Cage Morphology as a Highly Reversible Anode Material for Lithium-Ion Batteries. *Adv. Mater.* **2007**, *19*, 993−997.
(55) Grugeon, S.; Laruelle, S.; Herrera-Urbina, R.; Dupont, L.; Poizot, P.; Tarascona, J. M. Particle Size Effects on the Electrochemical Performance of Copper Oxides toward Lithium. *J. Electrochem. Soc.* **2001**, *148*, A285−A292.
(56) Yu, Y.; Chen, C. H.; Shui, J. L.; Xie, S. Nickel-Foam-Supported Reticular CoO-Li_2O Composite Anode Materials for Lithium Ion Batteries. *Angew. Chem., Int. Ed.* **2005**, *44*, 7085−7089.
(57) Yu, Y.; Shi, Y.; Chen, C. H. Nanoporous Cuprous Oxide/Lithia Composite Anode with Capacity Increasing Characteristic and High Rate Capability. *Nanotechnology* **2007**, *18*, 055706−055710.
(58) Poizot, P.; Laruelle, S.; Grugeon, S.; Dupont, L.; Tarascon, J. M. Nano-Sized Transition-Metal Oxides as Negative-Electrode Materials for Lithium-Ion Batteries. *Nature* **2000**, *407*, 496−499.
(59) Qin, J.; He, C. N.; Zhao, N. Q.; Wang, Z. Y.; Shi, C. S.; Liu, E. Z.; Li, J. J. Graphene Networks Anchored with Sn@Graphene as Lithium Ion Battery Anode. *ACS Nano* **2014**, *8*, 1728−1738.
(60) Wei, W.; Yang, S. B.; Zhou, H. X.; Lieberwirth, I.; Feng, X. L.; Müllen, K. 3D Graphene Foams Cross-Linked with Pre- Encapsulated Fe_3O_4 Nanospheres for Enhanced Lithium Storage. *Adv. Mater.* **2013**, *25*, 2909−2914.
(61) Xiao, Y.; Hu, C. W.; Cao, M. H. High Lithium Storage Capacity and Rate Capability Achieved by Mesoporous Co_3O_4 Hierarchical Nanobundles. *J. Power Sources* **2014**, *247*, 49−56.
(62) Cao, C.; Zhang, J. An Introduction to Electrochemical Impedance Spectroscopy. *Science, Beijing* **2002**, 86−106.
(63) Shin, J. W.; Ryu, W. H.; Park, K. S.; Kim, I. D. Morphological Evolution of Carbon Nanofibers Encapsulating SnCo Alloys and Its Effect on Growth of the Solid Electrolyte Interphase Layer. *ACS Nano* **2013**, *7*, 7330−7341.

DOI: 10.1021/acsami.5b02171
ACS Appl. Mater. Interfaces 2015, 7, 12840−12849